7-4-2014

Dual-Channel Red/Blue Fluorescence Dosimetry with Broadband Reflectance Spectroscopic Correction Measures Protoporphyrin IX Production during Photodynamic Therapy of Actinic Keratosis

Stephen Chad Kanick
Dartmouth College

Scott C. Davis
Dartmouth College

Yan Zhao
Dartmouth College

Tayyaba Hasan
Massachusetts General Hospital

Edward V. Maytin
Cleveland Clinic Lerner Research Institute

See next page for additional authors

Journal of Biomedical Optics

BiomedicalOptics.SPIEDigitalLibrary.org

Dual-channel red/blue fluorescence dosimetry with broadband reflectance spectroscopic correction measures protoporphyrin IX production during photodynamic therapy of actinic keratosis

Stephen Chad Kanick
Scott C. Davis
Yan Zhao
Tayyaba Hasan
Edward V. Maytin
Brian W. Pogue
M. Shane Chapman

SPIE.

Dual-channel red/blue fluorescence dosimetry with broadband reflectance spectroscopic correction measures protoporphyrin IX production during photodynamic therapy of actinic keratosis

Stephen Chad Kanick,[a,*,†] Scott C. Davis,[a,†] Yan Zhao,[a] Tayyaba Hasan,[b] Edward V. Maytin,[c] Brian W. Pogue,[a,b,d] and M. Shane Chapman[d]
[a]Thayer School of Engineering, Dartmouth College, Hanover, New Hampshire 03755
[b]Wellman Center for Photomedicine, Massachusetts General Hospital, Boston, Massachusetts 02114
[c]Biomedical Engineering, Cleveland Clinic, Cleveland, Ohio 44195
[d]Department of Surgery, Section of Dermatology, Dartmouth-Hitchcock Medical Center, Lebanon, New Hampshire 03766

Abstract. Dosimetry for aminolevulinic acid (ALA)-induced protoporphyrin IX (PpIX) photodynamic therapy of actinic keratosis was examined with an optimized fluorescence dosimeter to measure PpIX during treatment. While insufficient PpIX generation may be an indicator of incomplete response, there exists no standardized method to quantitate PpIX production at depths in the skin during clinical treatments. In this study, a spectrometer-based point probe dosimeter system was used to sample PpIX fluorescence from superficial (blue wavelength excitation) and deeper (red wavelength excitation) tissue layers. Broadband white light spectroscopy (WLS) was used to monitor aspects of vascular physiology and inform a correction of fluorescence for the background optical properties. Measurements in tissue phantoms showed accurate recovery of blood volume fraction and reduced scattering coefficient from WLS, and a linear response of PpIX fluorescence versus concentration down to 1.95 and 250 nM for blue and red excitations, respectively. A pilot clinical study of 19 patients receiving 1-h ALA incubation before treatment showed high intrinsic variance in PpIX fluorescence with a standard deviation/mean ratio of > 0.9. PpIX fluorescence was significantly higher in patients reporting higher pain levels on a visual analog scale. These pilot data suggest that patient-specific PpIX quantitation may predict outcome response. [DOI: 10.1117/1.JBO.19.7.075002]

Keywords: fluorescence; reflectance; optical spectroscopy; photodynamic therapy; dosimetry; pharmacokinetics; protoporphyrin IX.

Paper 140110R received Feb. 24, 2014; revised manuscript received May 6, 2014; accepted for publication May 27, 2014; published online Jul. 4, 2014.

1 Introduction

Aminolevulinic acid (ALA)-based photodynamic therapy (PDT) is an FDA-approved treatment for actinic keratosis (AK),[1] which starts as benign lesions from sun damage but can progress to squamous cell carcinoma if left untreated.[2] Multiple clinical investigations have found ALA-protoporphyrin IX (PpIX)-based PDT treatments to be an effective option for clearance of AK,[3–5] with 75 to 89% of patients reporting complete response. ALA-PpIX PDT is generally well tolerated and is not associated with scarring, which makes the treatment suitable for treating wide areas, especially given the high distribution of AK lesions on the sensitive skin of the face and scalp. The FDA-approved ALA-PpIX treatment protocol involves topical administration of ALA to the affected skin and incubation for 14 to 18 h. During incubation, the ALA penetrates into the tissue and disrupts the feedback mechanism of the porphyrin-synthetic pathway, resulting in excess generation of PpIX.[6] This process has been shown to result in increased production of PpIX in AK lesions compared with surrounding normal skin.[7] The subsequent administration of light results in photoactivation of PpIX, generating reactive oxygen species and leading to targeted tissue damage. However, incomplete treatment responses are often associated with thicker lesions[8,9] and are generally attributed to a combination of poor ALA penetration, insufficient PpIX generation, or inadequate light dose. A recent trend in the clinic toward the use of shorter ALA incubation times, administering the light dose at 1 to 3 h after topical ALA,[10–13] exacerbates the potential problem of incomplete responses. Shorter treatment protocols are now favored because of reduced time commitments for patients and clinic personnel and a more tolerable side-effect profile for patients. However, the pharmacokinetics of PpIX generation at very short contact times is not well characterized, and considering that ALA-incubation in skin has been reported to generate peak PpIX values between 6 and 24 h after ALA administration,[14,15] times shorter than this may increase the likelihood of insufficient PpIX generation, especially at deeper levels within lesions. The ability to identify potentially nonresponsive lesions before treatment could enable the physician to modify the protocol to improve outcomes, for example, by lengthening the incubation time or by adding an adjuvant[16,17] to improve PpIX production. The hurdle to achieving such customized therapy, however, is the

*Address all correspondence to: Stephen Chad Kanick, E-mail: stephen.c.kanick@dartmouth.edu

†These authors contributed equally to this work.

current lack of widely accepted and standardized methods to monitor depth-dependent PpIX generation in the skin. We have attempted to address this issue in the current paper.

Optical spectroscopy is one method that provides the capability to monitor PDT therapies. Measurements of PpIX fluorescence can inform an implicit metric[18] of the delivered therapeutic dose[19] if measurements are integrated throughout the treatment time. Several investigators have proposed ways to monitor ALA-induced PpIX levels during PDT (reviewed in Ref. 20), with many studies using fluorescence measurements to characterize the pharmacokinetics of PpIX production[7,14,15,21–24] and to monitor treatments.[24,25] However, classical approaches that use diffuse imaging of PpIX fluorescence provide assessments that are only qualitative, because diffuse signals must be averaged over large volumes, and the absolute values can be perturbed by background optical properties. One experimental approach to addressing this limitation has involved the design of custom fiber optic probes that localize the signal and mitigate the distortive influence of scattering and absorption. Probes have been designed to sample fluorescence with single fibers, which detect superficial fluorescence, thereby limiting the effect of absorption in the signal.[24,26] Model-based analysis can extract quantitative fluorescence from these measurements,[27,28] but this approach may not be suitable for sampling PpIX from beneath the epidermis (the outer layer of skin, which is highly scattering). Another approach is to use probes that sample remittance of multiple source-detector distances (from 200 to 1000 μm);[29] these have been used to return a localized and quantitative estimate of PpIX fluorescence. However, the algorithms utilized in this approach are only valid for conditions such as absorption dominated light transport, which is not sufficiently met in most skin studies.[30] Other investigators have developed a quantitative imaging approach that uses spectral imaging[31] or spatially modulated light[32,33] to provide images of quantitative PpIX fluorescence. However, spectral resolution of these approaches is not adequate to decouple the contribution of multiple fluorophores, including PpIX, photoproducts, and background tissue autofluorescence. While most probe- and imaging-based approaches estimate superficial fluorescence, algorithms have been designed to estimate depth-dependent PpIX production by coupling optical signals with an assessment of tissue structure (e.g., ultrasound).[34] However, these approaches sample a diffuse signal and provide a complex parametric representation of the sampled tissue volume. In addition to fluorescence, measurements of white light reflectance spectra have been used to monitor changes in the vasculature (e.g., blood flow, microvascular saturation). That information can be used to monitor patient-specific responses to PDT.[35,36]

In this paper, we report on a new multichannel, spectroscopic dosimeter developed to quantify PpIX fluorescence in skin. This probe-based system uses red and blue light excitation sources to distinguish PpIX fluorescence signals originating from different depths in tissue, which could prove to be an important capability for predicting responses *in vivo* and for customizing treatment parameters. The device also samples white light reflectance to inform an empirical correction factor that mitigates the distortive effects of background tissue optical properties on the collected PpIX fluorescence. Finally, the device also allows one to quantify parameters that describe the local vascular physiology, which could provide additional biomarkers predictive of response. Extensive phantom-based studies are presented that establish (1) the linearity of response and detection limits of the system; (2) the accuracy of the optical property estimation; and (3) the effect of white light correction on the fluorescence measurements. Finally, a 19-patient clinical pilot study is presented, which provides initial observations in dosimetry as related to initial estimates of treatment response.

2 Methods

2.1 *Dosimeter System*

A diagram and photographs of the probe-based experimental dosimeter are provided in Fig. 1. The system housed five illumination sources: four temperature-controlled laser diodes (405, 639, 735, and 785 nm, WorldStarTech, Toronto, Ontario) and an Ocean Optics HL-2000 Tungsten Halogen white light source (Ocean Optics, Dunedin, Florida). These sources were coupled to a motorized 6×1 fiber switch (DiConFiberoptics Inc., Richmond, California) through 200-μm fibers to enable rapid switching between channels. The output of the fiber switch was coupled to the patient's skin through an Ocean Optics R200-7-UV/VIS optical fiber probe that consisted of seven 200-μm fibers in the arrangement shown in Fig. 1(b). During measurements, the probe was held in contact with the patient's skin and light was delivered to the tissue through the central channel, shown in blue in Fig. 1(b). The six fibers surrounding the illumination fiber transmitted the remitted light through a motorized six-position filter wheel (ThorLabs FW102C, Newtown, New Jersey) and into an Ocean Optics USB4000 spectrometer with a spectral range between 346 and 1038 nm. The lasers, filter wheel, and spectrometer were USB-ready devices, while the DiCon fiber switch and white light source's internal shutter were controlled with an NI USB-6501 DAQ board. All control connections were consolidated in a powered USB hub connected to a laptop. The system was operated using a simple software interface written in Labview (National Instruments, Austin, Texas).

The PDT dosimetry measurements in this study were acquired with the white light source, 405 nm (blue channel) and 639 nm (red channel) laser diodes, and thus, the 735- and 785-nm laser diode channels were not used. Excitation filtering for fluorescence measurements was accomplished using a 1-mm-thick 435-nm color glass long-pass filter (Schott, Mainz) for blue channel excitation and a 650-nm long-pass interference filter (ThorLabs) for red excitation. The filters were selected to reduce, but not eliminate, the excitation signal to facilitate simultaneous measurement of the excitation and emission intensities in the same spectrum. While this was readily achievable with red channel excitation, the high attenuation of blue light in the presence of blood often reduced the blue light excitation signal to undetectable levels, even with low filtering efficiency.

Low-cost 635-nm laser diodes typically operate 2 to 4 nm above 635 nm, as was the case with the laser diode used in this system, so this was actually at 639 nm. Since the absorbance peak of PpIX falls off precipitously within this range, these lasers are rather inefficient at exciting PpIX fluorescence, a reality that results in relatively high minimum detectable PpIX concentrations. This is addressable by integrating 635-nm laser diodes with higher-wavelength tolerances at significantly higher cost.

Measurements were automatically acquired in the following sequence: (1) white light reflectance with no filtering, (2) red channel fluorescence, (3) blue channel fluorescence. To ensure

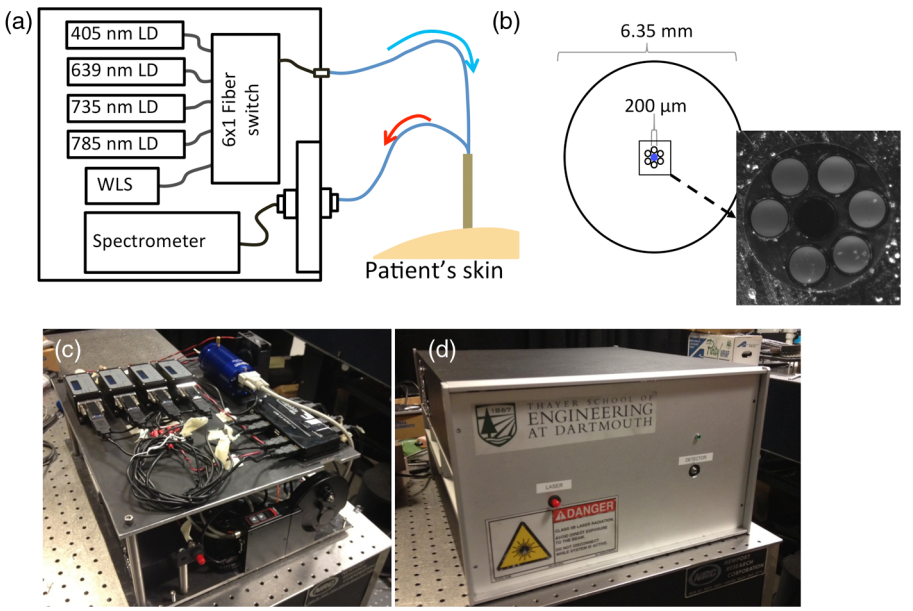

Fig. 1 (a) Schematic of the multichannel dosimeter setup showing system components. (b) Fiber arrangement of the patient-interface (probe tip), which is used in light compression contact-mode. The source fiber is represented in blue. The surrounding six fibers transmit light remitted from the tissue through the filter wheel and into the spectrometer. Photographs of the internal optical assembly and the chassis are shown in (c) and (d), respectively.

that measured spectra were within the dynamic range of the spectrometer, measurement exposure times were optimized automatically during the acquisition. This was achieved by acquiring a spectrum at an initial exposure time of 200 ms, checking that the measured signal was within a specified range and then either confirming the measurement was valid or automatically adjusting the acquisition time and repeating the measurement. The minimum and maximum times allowed were typically set at 10 and 1000 ms, respectively. Most fluorescence measurements were made at 300 or 50 ms, respectively, for blue and red channels, while white light measurements usually required 1 s. After each measurement, the fiber switch was positioned to a dark channel and a second spectrum acquired to allow real-time background subtraction of the ambient room light. Thus, a total of six spectra were recorded for an acquisition sequence of all three channels. The total acquisition time for this sequence was typically 25 s, limited primarily by the overhead in changing filter wheels and the long exposure time for the white light reflectance measurements. All measured spectra were background subtracted and corrected for exposure time before being analyzed using the protocols described below.

2.2 *White Light Reflectance Spectroscopy Data Processing*

Analyses of white light spectra were used for two purposes: (1) to correct the fluorescence measurements for the effects of optical propagation in tissue and (2) to estimate endogenous physiological parameters, such as whole blood volume fraction, oxygen saturation, and blood vessel density. The analysis was accomplished by applying a Monte Carlo–based look-up-table (LUT) approach similar to what has been reported previously[28,29] to relate measured light intensity to the wavelength-dependent optical properties within the sampled volume, including the absorption coefficient (μ_a) and the reduced scattering coefficient (μ_s'). In this study, LUT was generated for broadband light using validated Monte Carlo code[37] with the geometry configured to mimic the six discrete detector fibers interspaced around a central source fiber, as in Fig. 1(b). All fiber diameters were 0.2 mm and the source to detector spacing was set to 0.25 mm. Simulations assumed a homogenous medium with 20 values for μ_s', covering the range [0.1 to 50] mm^{-1}, and 13 values for μ_a, over the range of [0 to 10] mm^{-1}, resulting in 260 unique optical property combinations. Other simulation parameters include a Henyey-Greenstein phase function with anisotropy of g = 0.9, index of refraction of the medium = 1.37 and fibers = 1.45, and the numerical aperture of source and collection fibers = 0.22. Each simulation was initialized with 10^7 photons and returned the collected reflectance intensity.

Measured spectra were calibrated by relating the wavelength-dependent collected light intensity measured in a reference phantom composed of 2% Intralipid ($I_{\text{ref}}^{\text{meas}}$) to the LUT-based intensity returned for the known optical properties[38] of the phantom ($R_{\text{calib}}^{\text{LUT}}$). Thus, the calibration was given as

$$R_{\text{sample}}^{\text{meas}} = \frac{R_{\text{calib}}^{\text{LUT}}}{I_{\text{ref}}^{\text{meas}}} I_{\text{sample}}^{\text{meas}}. \quad (1)$$

This calibration converts collected light intensity measured in a sample ($I_{\text{sample}}^{\text{meas}}$) in units of counts/millisecond to reflectance ($R_{\text{sample}}^{\text{meas}}$) expressed in units of the percentage of launched photons that were collected from the Monte Carlo LUT.

After calibrating using Eq. (1), reflectance spectra were fit to an empirical relationship describing the effects of optical absorption and scatter on the remitted spectrum, a process that facilitated estimation of these parameters in the measured volume. Background scattering was estimated with a power-law function as

$$\mu_s' = a\left(\frac{\lambda}{\lambda_o}\right)^{(-b)}, \quad (2)$$

where a and b are the scatter amplitude and power, respectively. The background absorption coefficient, μ_a^{total}, was estimated from the sum of the product of chromophore concentrations and specific absorption coefficients within the sampled tissue volume. In skin, the dominant basis set of chromophores was specified to be hemoglobin and deoxygenated hemoglobin within whole blood, and melanin within the epidermis[30]

$$\mu_a^{\text{total}} = \sum(\mu_{a_i} c_i) = \mu_a^{\text{blood}} + \mu_a^{\text{melanin}}. \tag{3}$$

Here, the absorption coefficients of blood and melanin are given by μ_a^{blood} and μ_a^{melanin}, respectively. The absorption due to whole blood can be described by

$$\mu_a^{\text{blood}} = C_{\text{ves}}\text{BVF}[\text{Sat}\hat{\mu}_a^{\text{HBO2}} + (1 - \text{Sat})\hat{\mu}_a^{\text{HB}}], \tag{4}$$

where the volume fraction of blood is given by BVF, the specific absorption coefficients of oxygenated hemoglobin and deoxygenated hemoglobin are given as $\hat{\mu}_a^{\text{HBO2}}$ and $\hat{\mu}_a^{\text{HB}}$, and the contribution of each to the total absorption is given by the hemoglobin saturation (Sat). C_{ves} is a correction factor to account for the influence that the distribution of blood into discrete vessels has on the effective absorption.[39] $C_{\text{ves}} = \{[1 - e^{(-2\mu_a^{\text{blood}} r_v)}]/[2\mu_a^{\text{blood}} r_v]\}$, where r_v is the effective mean vessel radius.

For measurements performed on skin in the presence of melanin ($R_{\text{sample}}^{\text{skin,mel}}$), the attenuation attributable to the absorption of melanin was estimated using a Beer-Lambert based factor as

$$R_{\text{sample}}^{\text{skin}} = R_{\text{sample}}^{\text{skin,mel}} e^{\hat{\mu}_a^{\text{mel}} c_{\text{mel}} L_{\text{epi}}}, \tag{5}$$

where the exponential term containing the product of the specific absorption coefficient and concentration of melanin and the photon path length in the epidermis ($\hat{\mu}_a^{\text{mel}} c_{\text{mel}} L_{\text{epi}}$) acts as a filter on $R_{\text{sample}}^{\text{skin,mel}}$ to yield an estimate of reflectance in the absence of melanin absorption ($R_{\text{sample}}^{\text{skin}}$). This study assumed that $L_{\text{epi}} = 24\ \mu$m, approximating the path length of collected light within epidermis.[40] The melanin-free spectra from Eq. (5) was used within the fitting algorithm to estimate background optical properties (μ_s', μ_a^{blood}) in the tissue as described by Eqs. (2) to (4).

Prior to fitting, spectra were smoothed into discrete bins 5 pixels in width (equal to 1.5 nm), with a mean and standard deviation calculated within each bin. The smoothed reflectance spectra were fit over the [480 to 800] nm wavelength range, with light intensity <480 nm not included due to poor system transmission and sensitivity at those wavelengths. For measurements of skin, the algorithm estimated BVF, Sat, a, b, and c_{MEL}; r_v was unable to be fit as a free parameter, but was instead assumed to be 20 μm. For measurements of optical phantoms, the algorithm estimated BVF, Sat, a, and b, and did not include either melanin or C_{ves}. The spectral fitting algorithm was coded in MATLAB® using the *lsqnonlin* subroutine and the standard deviation of each binned pixel was used as a weighting factor. The algorithm also returned confidence intervals for fitted parameters as previously described[41] using *nlparci* subroutine. The qualities of spectral fits were quantified using a reduced chi-squared metric, $\chi^2 = \frac{1}{v}\sum[(R_{\text{data}} - R_{\text{model}})^2/\sigma^2]$.

2.3 *Fluorescence Spectral Analysis*

Quantifying fluorescence activity from the measured spectra generally followed a three-step process: (1) the raw spectra (after background subtraction and exposure time correction) were calibrated to the reference phantom, (2) these spectra were then corrected for the influence of optical properties using results from the white light spectroscopy measurements, and (3) a linear least squares spectral fitting routine decoupled the specific PpIX fluorescence from other fluorescent signals, such as autofluorescence and photoproducts. The details of this process are described here.

Collected fluorescence intensities $J_{\text{sample}}^{\text{meas}}(\lambda_x)$ were initially calibrated using

$$\text{FL}_{\text{sample}}^{\text{meas}}(\lambda_x) = \frac{J_{\text{sample}}^{\text{meas}}(\lambda_x)}{J_{\text{ref}}^{\text{meas}}(\lambda_{\text{calib}})}, \tag{6}$$

where $J_{\text{ref}}^{\text{meas}}(\lambda_{\text{calib}})$ is the collected fluorescence intensity measured in a reference phantom composed of 2% Intralipid. $J_{\text{ref}}^{\text{meas}}(\lambda_{\text{calib}})$ is evaluated at a single wavelength in the spectrum, with $\lambda_{\text{calib}} = [630, 680]$ nm for the source lasers [405, 639] nm, respectively. Both $J_{\text{sample}}^{\text{meas}}(\lambda_x)$ and $J_{\text{ref}}^{\text{meas}}(\lambda_{\text{calib}})$ are proportional to the product of the transmission efficiency of the system (T_{sys}), the intensity of the laser source (P_{source}), and the specific absorption coefficient ($\hat{\mu}_a^f$), concentration (c_f), and quantum efficiency (Q_f) of the sampled fluorophore. Equation (6) assumes that the product $\hat{\mu}_a^f c_f Q_f$ is standardized by the reference phantom, such that daily variations in coupling efficiency of the probe setup or fluctuations in laser intensity ($T_{\text{sys}} P_{\text{source}}$) will be reflected in both $J_{\text{sample}}^{\text{meas}}(\lambda_x)$ and $J_{\text{ref}}^{\text{meas}}(\lambda_{\text{calib}})$, and allow these factors to cancel out in the resulting $\text{FL}_{\text{sample}}^{\text{meas}}(\lambda_x)$ spectra, which is given in dimensionless units.

Next, the calibrated fluorescence spectrum, $\text{FL}_{\text{sample}}^{\text{meas}}(\lambda_x)$, is corrected for the influence of background optical properties by using an empirical correction factor based on sampled reflectance intensities, which is an approach described extensively,[31,42–44] and is given as

$$\text{FL}_{\text{sample}}^{\text{corr}}(\lambda_x) = \frac{\text{FL}_{\text{sample}}^{\text{meas}}(\lambda_x)}{R_x^{\kappa} R_m^{\alpha}}, \tag{7}$$

where $\text{FL}_{\text{sample}}^{\text{corr}}(\lambda_x)$ is the corrected fluorescence spectrum, and R_x and R_m represent reflectance intensity in the excitation and emission wavebands. Here, R_x and R_m were evaluated by averaging model fitted estimates of reflectance within specified wavebands. For blue excitation, R_x was evaluated over [400 to 410] nm, R_m over [630 to 640] nm, and $[\kappa, \alpha]$ was found to be [0.7, −0.7]. For red excitation, R_x was evaluated over [634 to 641] nm, R_m over [695 to 705] nm, and $[\kappa, \alpha]$ was found to be [1.0, −0.7]. Values for exponents were evaluated by minimizing the error from PpIX fluorescence recovered between measurements of $\text{FL}_{\text{sample}}^{\text{corr}}(\lambda_x)$ in optical phantoms with a wide range of absorption and scattering properties.

Once corrected for optical properties, $\text{FL}_{\text{sample}}^{\text{corr}}(\lambda_x)$ spectra were analyzed as a linear combination of basis spectra representing tissue autofluorescence, PpIX fluorescence, and PpIX photoproduct (PP) fluorescence. For blue excitation, the emission was fit by

$$\text{FL}_{\text{sample}}^{\text{corr}}(\lambda_{\text{blue}}) = c_{\text{auto}}^{\text{blue}}\zeta_{\text{auto}} + c_{\text{ppIX}}^{\text{blue}}\zeta_{\text{PpIX}} + c_{\text{PP1}}^{\text{blue}}\zeta_{\text{PP1}} + c_{\text{PP2}}^{\text{blue}}\zeta_{\text{PP2}}, \tag{8}$$

where $[\zeta_{\text{auto}}, \zeta_{\text{PpIX}}, \zeta_{\text{PP1}}, \zeta_{\text{PP2}}]$ are the basis spectra and $[c_{\text{auto}}^{\text{blue}}, c_{\text{PpIX}}^{\text{blue}}, c_{\text{PP1}}^{\text{blue}}, c_{\text{PP2}}^{\text{blue}}]$ are the contribution of fluorescence

of the tissue autofluorescence, PpIX, and PpIX photoproducts PP1 and PP2. The photoproducts included here were previously defined[45] and are constructed using a Gaussian centered at [652, 671] nm with width [15, 27] nm for [PP1, PP2], respectively. For red excitation, the emission waveband was not sensitive enough to photoproducts to characterize them individually, and thus, Eq. (8) was simplified to

$$\mathrm{FL}^{\mathrm{corr}}_{\mathrm{sample}}(\lambda_{\mathrm{red}}) = c^{\mathrm{red}}_{\mathrm{auto}}\zeta_{\mathrm{auto}} + c^{\mathrm{red}}_{\mathrm{ppIX}}\zeta_{\mathrm{PpIX}} + c^{\mathrm{red}}_{\mathrm{background}}, \quad (9)$$

where a third-order polynomial, $c^{\mathrm{red}}_{\mathrm{background}} = c^{\mathrm{red}}_{b1}\lambda + c^{\mathrm{red}}_{b2}\lambda^2 + c^{\mathrm{red}}_{b3}\lambda^3$, was included to characterize photoproduct fluorescence and mismatch in the spectral features of the background autofluorescence and the sampled autofluorescence basis spectrum; incorporation of $c^{\mathrm{red}}_{\mathrm{background}}$ substantially improved fit quality.

Prior to fitting, the calibrated fluorescence spectra were reduced into discrete bins 5 pixels in width (equal to 1.5 nm), with a mean and standard deviation calculated within each bin. The fitted waveband for $\mathrm{FL}^{\mathrm{corr}}_{\mathrm{sample}}(\lambda_{blue})$ was [600 to 800] nm and that for $\mathrm{FL}^{\mathrm{corr}}_{\mathrm{sample}}(\lambda_{\mathrm{red}})$ was [675 to 800] nm. The fitting algorithm was coded in a MATLAB® script and used the *lsqnonlin* subroutine to perform a Levenberg-Marquardt least squares fitting regime that minimized the error between model predictions and measured data, with each pixel weighted by the standard deviation. The fitting procedure returned estimates and confidence intervals of $[c^{\mathrm{blue}}_{\mathrm{auto}}, c^{\mathrm{blue}}_{\mathrm{PpIX}}, c^{\mathrm{blue}}_{\mathrm{PP1}}, c^{\mathrm{blue}}_{\mathrm{PP2}}]$ for blue and $[c^{\mathrm{red}}_{\mathrm{auto}}, c^{\mathrm{red}}_{\mathrm{PpIX}}, c^{\mathrm{red}}_{b1}, c^{\mathrm{red}}_{b2}, c^{\mathrm{red}}_{b3}]$ for red excitation.

To show the increased accuracy enabled by spectral fitting, we also examined the simple integral of the corrected fluorescence spectra $\mathrm{Area}^{\mathrm{source}}_{\mathrm{PpIX}}$ over a waveband of the remission spectra, essentially bypassing the spectral fitting algorithm (the final step in the analysis process). The *trapz* subroutine in MATLAB® was used to numerically integrate $\mathrm{FL}^{\mathrm{corr}}_{\mathrm{sample}}(\lambda_{\mathrm{blue}})$ over [620 to 720] nm, and $\mathrm{FL}^{\mathrm{corr}}_{\mathrm{sample}}(\lambda_{\mathrm{red}})$ over [680 to 720] nm, providing estimates of $\mathrm{Area}^{\mathrm{blue}}_{\mathrm{PpIX}}$ and $\mathrm{Area}^{\mathrm{red}}_{\mathrm{PpIX}}$, respectively.

2.4 *System Validation Using Tissue-Simulating Phantoms*

Phantom experiments were used to achieve four objectives: (1) characterize the linearity of response to PpIX concentration for both fluorescence channels, (2) determine the minimum detectable concentration of PpIX for both fluorescence channels, (3) determine the accuracy of the white light reflectance analysis in estimating scattering parameters and chromophore concentrations, and (4) examine the stability of the fluorescence measurements to background optical properties with and without correction. Phantoms were constructed using Intralipid (20% Frenius-Kabi, Bad Homburg, Germany), bovine whole blood (7200811 Lampire Biological Inc., Pipersville, Pennsylvania), and PpIX (P8293, Sigma-Aldrich, St. Louis, Missouri). All phantoms were composed of 5% Tween20 (P1379, Sigma-Aldrich) to mitigate aggregation. To explore linearity of response and minimum detection limits of PpIX fluorescence, measurements were acquired in phantoms composed of 1% Intralipid, and 1% BVF, and over a range of $[\mathrm{PpIX}] = [0.122, 0.244, 0.488, 0.977, 1.95, 3.90, 7.80, 15.6, 31.3, 62.5, 125, 250, 500, 1000, 2000, 4000]$ nM. To examine accuracy of white light reflectance analysis and stability to changes in optical properties, measurements were acquired in phantoms prepared using volume fractions of Intralipid [1, 2, 3] % and whole blood [0.5, 1, 2, 3] %. This resulted in 12 phantom combinations, each of which was sampled using serial dilutions of PpIX to achieve $[\mathrm{PpIX}] = [15.6, 62.5, 250, 1000, 4000]$ nM. For each phantom composition, white light reflectance, and blue- and red-excited fluorescence measurements were acquired, and measurements were repeated three times. To determine the lower limit of detection for each fluorescence metric ($c^{\mathrm{blue}}_{\mathrm{PpIX}}$, $c^{\mathrm{red}}_{\mathrm{PpIX}}$, $\mathrm{Area}^{\mathrm{blue}}_{\mathrm{PpIX}}$, $\mathrm{Area}^{\mathrm{red}}_{\mathrm{PpIX}}$), the data were fit to a line forced through zero, and the lower limit was identified as the highest [PpIX] at which the metric deviated >25% from the fit. Estimated optical parameters were compared with known phantom properties (i.e., BVF and μ_s') using the Pearson correlation coefficient (r) to show linearity, and the mean residual was calculated as $\overline{\mathrm{resid}} = 100[(\mathrm{estimated} - \mathrm{known})/\mathrm{estimated}]$.

2.5 *Pilot clinical Study*

A clinical feasibility study was conducted to establish the feasibility of using the device, to determine initial metrics of system performance, and to acquire information about interpatient variability. The study was approved by the institutional review board, and 19 patients with AK, identified in a standard clinical dermatology practice (MS Chapman, Dartmouth Hitchcock Medical Center), were enrolled. Informed consent was obtained in writing from patients prior to initiation of treatment. PDT procedure began with topical application of ALA (Levulan Kerastick, DUSA Pharmaceuticals, Wilmington, Massachusetts) to the lesion area. Patients were instructed to wait for 1 h in the outpatient waiting room, with care taken to avoid exposure to direct sunlight. Patients were treated with a noncoherent blue light source (BLU-U Blue Light Photodynamnic Therapy Illuminator, DUSA Pharmaceuticals) with the prescribed exposure of 10 J/cm^2 (8 to 15 min) for each patient. Immediately following treatment, patients were asked to assess their maximal pain level experienced during treatment using the visual analog scale (VAS) from 0 to 10; this was recorded as an assessment of treatment response in this study. Optical measurements were performed at three time points during the treatment protocol: (1) prior to administration of ALA, (2) following 1-h incubation with ALA and before light illumination, and (3) immediately following administration of the treatment light dose. All measurements were recorded with the probe tip in gentle contact with the surface of the AK lesion. Fluorescence measurements prior to ALA administration were used to record patient-specific basis spectra for the tissue autofluorescence and were used in the spectral fitting algorithms described in Eqs. (8) and (9).

Optical spectra recorded were checked for integrity using the fit quality metric χ^2. Fluorescence measurements from patients prior to ALA administration were used to determine a patient-specific basis spectra for the tissue autofluorescence. Analysis of optical spectra from patients provided information about PpIX generation and PDT dose as well as vascular changes in response to PDT.

2.6 *PDT Dose Metrics for Pilot Clinical Data*

Optical measurements of PpIX fluorescence were used to estimate metrics of the therapeutic dose delivered during treatment. Assuming that the dose can be characterized by observed changes to PpIX fluorescence (and that adequate oxygen was either supplied by perfusion or diffusion through the skin), the dose is proportional to the amount of PpIX consumed through photobleaching during treatment, as shown previously.[25] The absolute photodynamic dose was calculated as

$$\text{Dose}_{\text{PpIX}}^{\text{source}} = c_{\text{PpIX}}^{\text{source}}(\text{PreTx}) - c_{\text{PpIX}}^{\text{source}}(\text{PostTx}), \quad (10)$$

where the superscript source represents both the blue and red excitation channels. The amount of photobleaching, PB_{PpIX}, was calculated as a percent change from the pretreatment measurement as

$$\text{PB}_{\text{PpIX}}^{\text{source}} = 100\left[\frac{c_{\text{PpIX}}^{\text{source}}(\text{PreTx}) - c_{\text{PpIX}}^{\text{source}}(\text{PostTx})}{c_{\text{PpIX}}^{\text{source}}(\text{PreTx})}\right], \quad (11)$$

which again was calculated for excitation using both blue, $\text{PB}_{\text{PpIX}}^{\text{blue}}$, and red, $\text{PB}_{\text{PpIX}}^{\text{red}}$, channels.

The relationship between the two fluorescence channels was also examined by calculating a ratio-based metric of PpIX fluorescence intensity sampled by the red and blue channels as

$$\text{Ratio}_{\text{RB}} = \frac{c_{\text{PpIX}}^{\text{red}}}{c_{\text{PpIX}}^{\text{blue}}}, \quad (12)$$

where Ratio_{RB} is given as the ratio of PpIX fluorescence sampled from deep to shallow depths (red to blue) within the optically sampled skin volume that qualitatively characterizes PpIX distribution.

Patient-reported pain was used as a preliminary response metric in this pilot study. Metrics of PDT dose and patient-reported pain were compared statistically using a Kruskal–Wallis one-way analysis of variance, with significance associated with $p < 0.05$.

2.7 *Depth Sensitivity Analysis Using Monte Carlo Simulations*

In order to characterize the origin depth of PpIX fluorescence sampled using the blue and red channels, we performed a set of Monte Carlo simulations. The simulation geometry approximated the optical property distribution in the skin as a seven-layer structure, as described previously in Ref. 40, and considered three cases with varying spatial distributions of PpIX within the tissue. Case 1 included homogenous PpIX throughout all of the tissue volume with $\mu_{\text{af}}^{\text{PpIX}}$ selected to approximate [PpIX] = 1000 nM. Case 2 considered superficially distributed PpIX, with the absorption of PpIX at deeper depths ($Z < 300$ μm) decreased by a factor of 7, while the PpIX at shallow depths was unchanged. Case 3 considered deeply distributed PpIX, with the absorption of PpIX at shallow depths ($Z > 300$ μm) decreased by a factor of 7, while the PpIX at deeper depths was unchanged. The simulations were performed using validated Monte Carlo code;[46] each simulation initialized 10^7 photons. The collected fluorescence intensity for the measurement and depth of origin for each collected fluorescence photon were recorded and used to estimate the 80% sampling depth ($Z_{\text{FL}}^{80\%}$) using the quantile subroutine in MATLAB®.

3 Results

3.1 *Tissue Phantom Measurements*

3.1.1 *Linearity of fluorescence response*

To characterize the response of the dosimeter system to changes in PpIX concentration ([PpIX]) and to establish the limits of detection, measurements were acquired in tissue phantoms composed of Intralipid 1% and whole blood 1% and [PpIX] ∈ [0.1 to 4000] nM. Figure 2(a) shows a representative fluorescence spectrum resulting from blue light excitation for a phantom containing [PpIX] = 500 nM, and the corresponding model fit. The plot shows the fitted contributions of background tissue autofluorescence, PpIX, and the very small contributions from photoproducts to the total fluorescence. $c_{\text{PpIX}}^{\text{blue}}$ versus [PpIX] data are shown on linear [Fig. 2(b)] and log [Fig. 2(c)] scales to illustrate the quality of the linear relationship over a wide range of [PpIX] values. The log-scale plot in Fig. 2(c) allows identification of the lower limit of detection of $c_{\text{PpIX}}^{\text{blue}}$ at 1.95 nM, below which the $c_{\text{PpIX}}^{\text{blue}}$ versus [PpIX] relationship deviates from linearity. For comparison, Fig. 2(d) shows the integrated metric of fluorescence ($\text{Area}_{\text{PpIX}}^{\text{blue}}$), which does not utilize spectral fitting and results in an elevated lower limit of detection of 250 nM. This substantial difference in sensitivity is due to the fitting algorithm adequately decoupling fluorescence from PpIX and background fluorophores, while the integrated metric is confounded by these factors at low [PpIX] values.

The data in Fig. 3 show the fluorescence response of the same phantom set as in Fig. 2 measured with the red excitation laser. Figure 3(a) shows representative measured and fitted spectra for [PpIX] = 1000 nM. The data in Figs. 3(b) and 3(c) show a linear response for $c_{\text{PpIX}}^{\text{red}}$ versus [PpIX] from [250 to 4000] nM and Fig. 3(d) shows the $\text{Area}_{\text{PpIX}}^{\text{red}}$ versus [PpIX]. Lower limits of PpIX detection for the red channel were identified for both spectral fitting (250 nM) and integrated fluorescence (1000 nM). The sensitivity of the system to red channel fluorescence is far lower than for blue light excitation, which is attributable to the absorption coefficient of PpIX being ~30-fold higher at 405 nm than at 639 nm.

3.1.2 *White light spectroscopy*

Optical measurements were performed in 12 sets of tissue-simulating phantoms with different amounts of Intralipid (volume fraction= [1 to 3]%) and whole blood (BVF= [0.5 to 3]%) to yield biologically relevant scattering and absorption properties. Figure 4(a) shows an example of a measured white light spectrum sampled in phantom with 1% Intralipid and 1% BVF. The black circles indicate measured data points and the corresponding model fit is shown in the red line. Differences between data and model fits are shown in the residual displayed below the spectrum. Figure 4(b) shows the estimated versus known μ_s' at two wavelengths [440, 639] nm. The scattering estimates showed a linear relationship versus known values in all phantoms (slope = 1.00, $r = 0.99$), with a mean residual between model estimates and the linear fit of $\overline{\text{resid}}(\mu_s') < 3\%$. Figure 4(c) shows the estimated versus known BVF with a linear relationship (slope = 0.98, $r = 0.98$) over the range BVF= [0.5 to 3]% and mean residual $\overline{\text{resid}}(\text{BVF}) < 15\%$.

3.1.3 *Fluorescence correction for optical property distortion*

Optical measurements of the 12 different combinations of absorption and scattering were used to examine the influence of optical properties on estimates of PpIX fluorescence and the capacity to correct for these effects. Figure 5(a) shows the variation of raw PpIX fluorescence estimated from $\text{FL}_{\text{sample}}^{\text{uncorr}}(\lambda_{\text{blue}})$ among the 12 phantoms. Here residual error is expressed as the percentage difference between the PpIX fluorescence estimated in each phantom and the average of all phantoms; each phantom contains the same amount of [PpIX], i.e.,

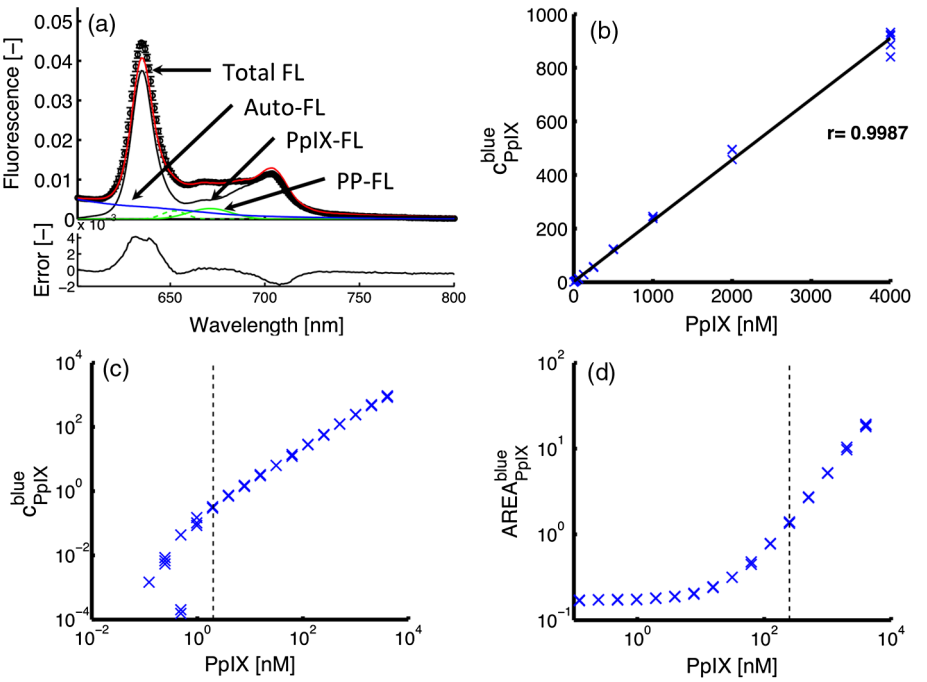

Fig. 2 Fluorescence measurements in protoporphyrin IX (PpIX) dilution series as measured with blue excitation light. Phantoms were constructed with Intralipid 1%, whole blood 1%, and Tween 5%. (a) A representative spectral fit is shown for [PpIX] = 500 nM. Sixteen dilutions were sampled between 4000 nm and 0.1 nM. The fitted PpIX fluorescence versus known PpIX concentration is shown (b) on a linear scale and (c) on a log scale with the lower limit of detection identified at 1.95 nM. The integrated fluorescence area versus PpIX concentration is shown in (d) with the lower limit of detection identified at 250 nM.

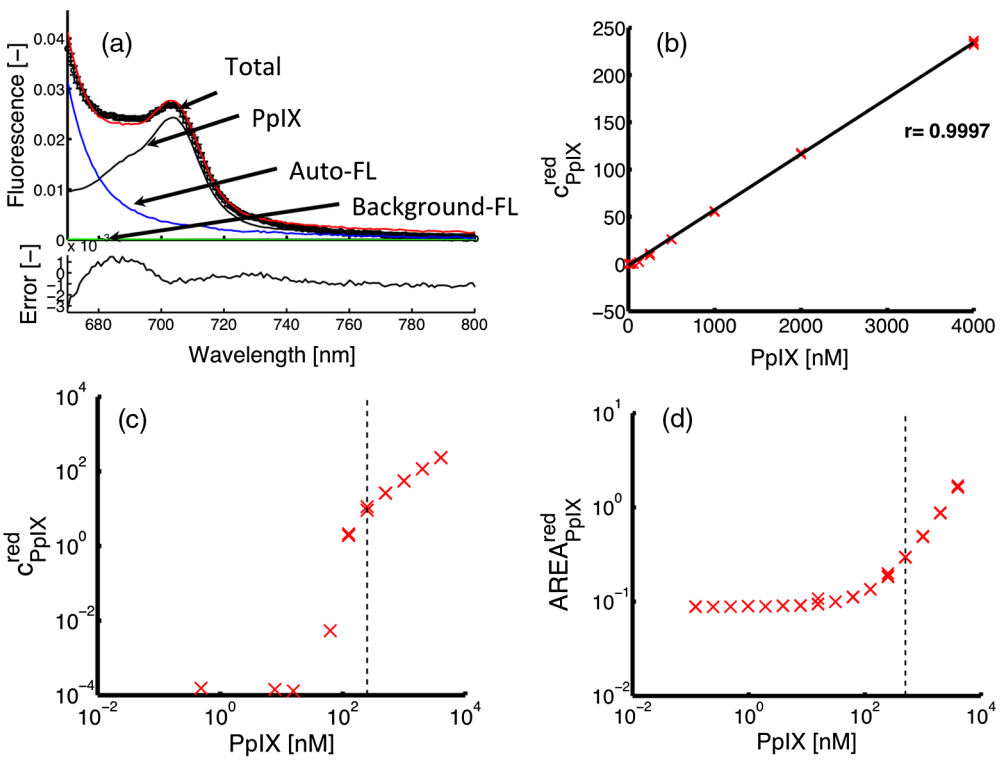

Fig. 3 Fluorescence measurements in PpIX dilution series as measured with red excitation light. Phantoms were constructed with Intralipid 1%, whole blood 1%, and Tween 5%. (a) A representative spectral fit is shown for [PpIX] = 1000 nM. Sixteen dilutions were sampled between 4000 nm and 0.1 nM. The fitted PpIX fluorescence versus known PpIX concentration is shown (b) on a linear scale and (c) on a log scale with the lower limit of detection identified at 250 nM. The integrated fluorescence area versus PpIX concentration is shown in (d) with the lower limit of detection identified at 1000 nM.

1000 nM. These data show that the raw fluorescence is substantially distorted by variations in background scattering and absorption, with $\overline{\text{resid}} < 37\%$. Figure 5(b) shows residual error for corrected PpIX fluorescence, estimated from $\text{FL}^{\text{corr}}_{\text{sample}}(\lambda_{\text{blue}})$ as given in Eq. (5). Comparison of Figs. 5(a) and 5(b) shows a reduction in error, with $\overline{\text{resid}}$ dropping to <9% for the corrected estimates of PpIX. Figures 5(c) and 5(d) show uncorrected and corrected PpIX fluorescence estimated from the red channel, with an improvement in $\overline{\text{resid}}$ values from <20 to <8% provided by the optical property correction factor. Inspection of the error plots do not show a trend with either Intralipid or whole blood, indicating that the resulting corrected estimates of PpIX are insensitive to variations in both scattering and absorption.

3.2 *Pilot Clinical Data*

3.2.1 *Clinical PDT observations*

Of the 19 patients enrolled in the study, 15 were used in this analysis; two were excluded due to an instrument error (IDs 10 and 11), and one patient was excluded due to a sampled BVF that exceeded the absorption bounds of the LUT (ID 2). Additionally, data from one patient showed erroneous features in the spectra (ID 8), which were identified by a metric of fit quality ($\chi^2 > 3$) and are likely due to confounding environmental influences (e.g., sufficient coupling to skin surface, influence of room lights, movement artifacts, etc.). Figure 6 shows pain assessed on the VAS immediately following PDT treatment, with 12 of 15 patients reporting nonzero

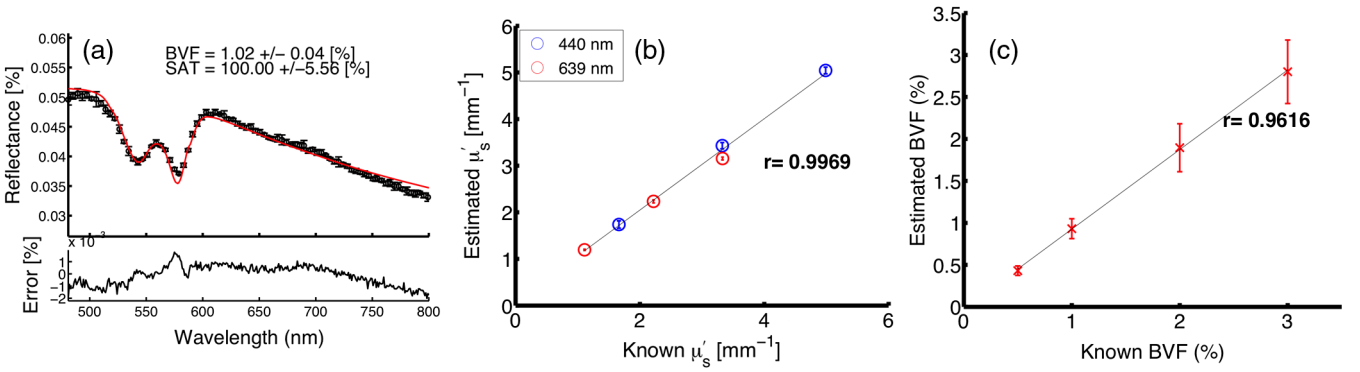

Fig. 4 (a) Representative white light spectra sampled in tissue phantoms for Intralipid 1% and blood volume of 1%. Estimated versus known values for (b) reduced scattering coefficient at blue and red excitation wavelengths and (c) blood volume fraction. Error bars on (b) and (c) represent variation between phantoms.

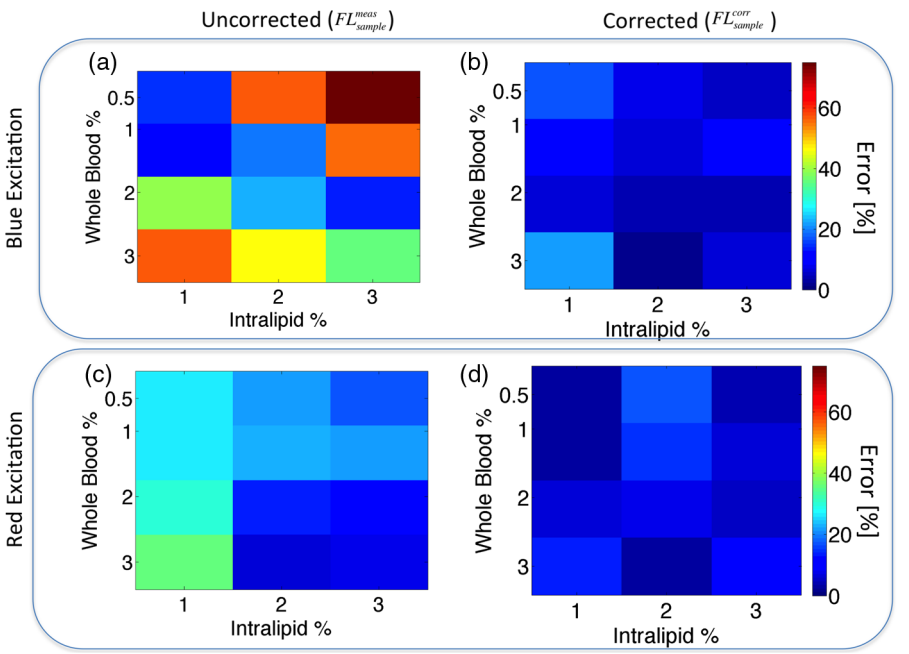

Fig. 5 (a) and (b) The residual error between fitted PpIX fluorescence emission spectra excited by blue excitation light for uncorrected and corrected spectra, respectively. (c) and (d) The residual error between fitted PpIX fluorescence emission spectra excited by red excitation light. Residual is calculated as the percentage deviation for fitted PpIX fluorescence normalized to average of estimates from all phantoms.

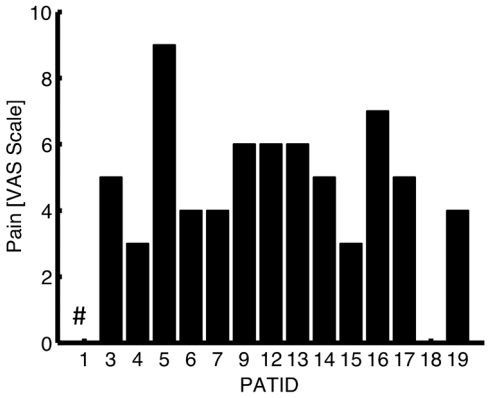

Fig. 6 Visual analog scale (VAS) pain as reported by patients immediately after photodynamic therapy (PDT) treatment. # indicates that pain was not assessed on ID1.

pain; $\overline{\text{pain}} = 4.8 +/- 2.3$, range = [0 to 9]. While the number of patients is small, the reported pain approximates a normal distribution and spans the full VAS range.

Figure 7 shows representative fluorescence and white light spectra measured from the AK lesion on patient ID 1. Fluorescence spectra sampled from the lesion using both blue and red excitation sources show strong PpIX fluorescence emission prior to treatment light delivery [Figs. 7(a) and 7(c), respectively], while post-treatment fluorescence activity was much reduced [Figs. 7(b) and 7(d)]. The associated photobleaching rates were $\text{PB}_{\text{PpIX}}^{\text{blue}} = 97\%$ and $\text{PB}_{\text{PpIX}}^{\text{red}} = 100\%$. White light reflectance spectra presented in Figs. 7(e) and 7(f) show differences in vascular physiology between pre- and post-Tx, with increases in BVF and Sat observed. The analysis presented in Fig. 7 is representative of the spectral fits performed on most of the patients enrolled in the study.

Figure 8(a) shows PpIX fluorescence excited by blue light measured before and after light treatment for each patient. These data show substantial interpatient variability in the accumulation of PpIX after the 1-h incubation time; $\bar{c}_{\text{PpIX}}^{\text{blue}} = 3.4 +/- 3.1$, range = [0 to 9.3]. For patients with nonzero PpIX fluorescence, the majority of PpIX was consumed during treatment with high observed photobleaching rates $\overline{\text{PB}}_{\text{PpIX}}^{\text{blue}} = 89 +/- 11\%$, range = [62 to 100] %, and thus, the absolute dose ($\text{Dose}_{\text{PpIX}}^{\text{blue}}$) closely followed the pre-Tx PpIX fluorescence, with $\overline{\text{Dose}}_{\text{PpIX}}^{\text{blue}} = 24.7 +/- 22.5$. When patient-reported pain after treatment was grouped into high (VAS >= 5) and low (VAS < 5) pain, both $c_{\text{PpIX}}^{\text{blue}}$ and $\text{Dose}_{\text{PpIX}}^{\text{blue}}$ were predictive of treatment-induced pain (with $p < 0.01$ for both), with the latter shown in Fig. 8(b). Figure 8(c) shows that the photobleaching expressed as a percentage of pre-Tx ($\text{PB}_{\text{PpIX}}^{\text{blue}}$) did not show a significant indication for patient-reported pain ($p < 0.24$); it should be noted that this analysis of photobleaching included zero values for undetectable PpIX.

A similar analysis was completed for the red channel fluorescence measurements, as shown in Fig. 9. These data also show substantial interpatient variability in pre-Tx PpIX accumulation of PpIX($\bar{c}_{\text{PpIX}}^{\text{red}} = 2.9 +/- 2.8$, range = [0 to 9.1]) and substantial photobleaching ($\overline{\text{PB}}_{\text{PpIX}}^{\text{blue}} = 8.9 +/- 17\%$, range = [46 to 100] %). While less significant than for the blue channel measurements, both $c_{\text{PpIX}}^{\text{red}}$ and $\text{Dose}_{\text{PpIX}}^{\text{red}}$ showed a significant difference for patients reporting low and high pain ($p < 0.03$ and $p < 0.04$), which was also not observed for the calculated photobleaching values, $\text{PB}_{\text{PpIX}}^{\text{red}}$ ($p < 0.09$).

Analysis of white light spectra returned quantitative descriptions of tissue composition and vascular physiology. Figure 10 shows optical tissue parameters for all patients before and after light treatment. The observed average values of these parameters for pretreatment measurements and the change in values after treatment are blood volume fraction $\overline{\text{BVF}} = 0.9 +/- 1.1$ (%) and $\overline{\Delta\text{BVF}} = 0.0 +/- 1.0$ (%) [Fig. 10(a)]; microvascular saturation $\overline{\text{SAT}} = 42 +/- 36$ (%) and $\overline{\Delta\text{SAT}} = 16 +/- 48$ (%) [Fig. 10(b)]; reduced scattering coefficient $\bar{\mu}_s'(639\,\text{nm}) = 2.1 +/- 0.3\,\text{mm}^{-1}$ and $\Delta\bar{\mu}_s'(639\,\text{nm}) = 0.1 +/- 0.3\,\text{mm}^{-1}$ [Fig. 10(c)]; and melanin fraction in epidermis $\bar{c}_{\text{MEL}} = 14 +/- 3$ (%) and $\overline{\Delta c}_{\text{MEL}} = 1.6 +/- 4.6$ (%) [Fig. 10(d)]. Comparing changes in physiological parameters with PDT dose metrics showed a moderate inverse correlation between the change in BVF and pain ($r = -0.55$ m, $p < 0.08$), and a moderate positive correlation between $\text{Dose}_{\text{PpIX}}^{\text{blue}}$ and the change in hemoglobin saturation ($r = 0.44$, $p < 0.08$); those correlations were not significant in this small study.

3.2.2 *Depth sensitivity of analysis of two-color PpIX measurement*

PpIX fluorescence intensities sampled by both blue and red excitation on each lesion were highly correlated ($r = 0.90$, $p < 0.001$). A ratiometric comparison of red to blue PpIX fluorescence (Ratio_{RB}) showed substantial interpatient variability ($\overline{\text{Ratio}}_{\text{RB}} = 0.92 +/- 0.51$, range = [0.23 to 2.23]), as shown in Fig. 11(a). It should be noted that Ratio_{RB} was calculated only for patients showing detectable PpIX before treatment, excluding three additional patients from this analysis. In principle, Ratio_{RB} should reveal coarse information on the depth of the PpIX distribution, with larger Ratio_{RB} values associated with PpIX fluorescence originating from deeper depths within the skin tissue; however, this has not been shown explicitly. Interestingly, Ratio_{RB} was an indicator of pain, with elevated Ratio_{RB} values significantly higher for patients reporting lower pain; this is shown in Fig. 11(b).

A series of simulations were performed to characterize the sensitivity of two-color fluorescence measurements of PpIX to the depth-dependent distribution of PpIX in the skin. The simulation results are summarized in Fig. 12. Case 1 simulates homogenously distributed PpIX, with red channel sampling PpIX from 3+-fold deeper than the blue and the ratio of red to blue fluorescence intensities normalized to 1. Case 2 considers superficially distributed PpIX; here, both channels sample superficial PpIX. The decrease in deeper PpIX resulted in a disproportionate decrease in intensity sampled with red compared with blue (with 74 and 10% reductions in red and blue intensities), such that the resulting Ratio_{RB} decreased to 0.3. Case 3 considers deeply distributed PpIX; here, the signal sampled from both channels now originates from deeper layers. The decrease in superficial PpIX saw intensity sampled with blue decreased much more than with red (with 80 and 15% reductions in blue and red intensities), yielding an increase of Ratio_{RB} to 4.4. These data indicate that the ratiometric analysis of PpIX fluorescence sampled by red and blue channels can provide a qualitative description of the PpIX distribution, with larger values of Ratio_{RB} associated with more deeply distributed PpIX and, conversely, smaller values of Ratio_{RB} associated with superficially distributed PpIX.

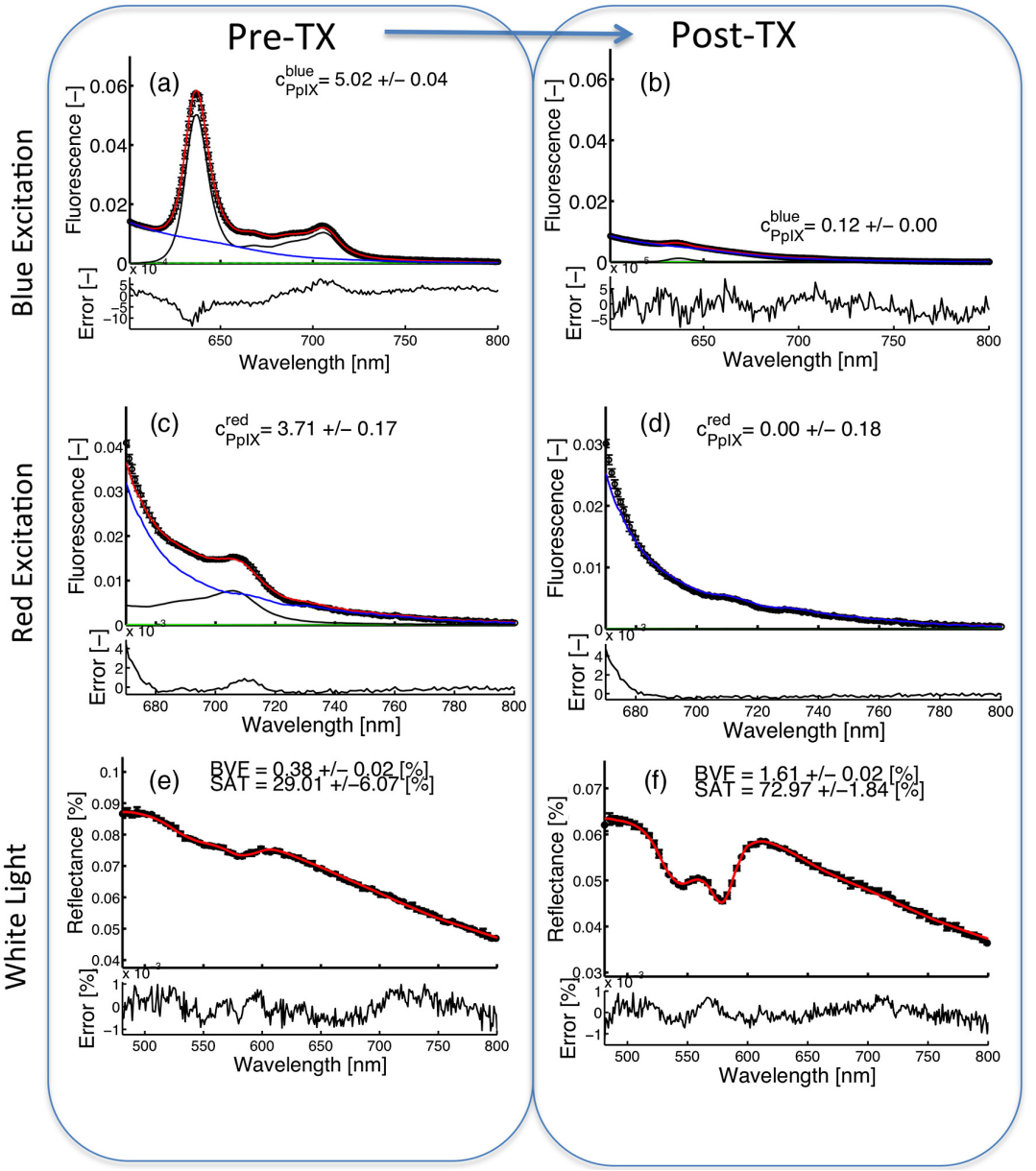

Fig. 7 Representative optical measurements of fluorescence emission with excitation with (top) blue, (middle) red, and (bottom) white light reflectance from patient ID1. Left-hand panels show measurements 1 h following aminolevulinic acid administration (pre-Tx). Right-hand panels show measurements immediately after administration of treatment light (post-Tx).

4 Discussion

This study introduced a novel spectrometer-based optical dosimetry system designed to monitor and ultimately improve response rates of short-contact ALA-PpIX PDT treatments of AK. The fiber switching capabilities of the instrument allow sequential measurements with a variety of illumination sources, including a white light source for reflectance spectroscopy and a variety of laser sources to excite fluorophores in the tissue. In this study, the instrument was configured to acquire PpIX fluorescence using blue (405 nm) and red (639 nm) excitation sources, a novel approach for PDT dosimetry, which facilitates estimation of PpIX activity at different depths. Measurements acquired in optical phantoms revealed an extremely linear response to changes in PpIX concentration down to the minimum detectable concentrations of 1.95 nM (for blue excitation) and 250 nM (for red excitation). Achieving these detection limits required the use of spectral fitting algorithms to extract PpIX fluorescence from the contaminating effects of autofluorescence and photoproducts. Without spectral fitting, detectable limits rose to 250 and 1000 nM for the blue and red channels, respectively. The difference in sensitivity between these channels is primarily due to the difference in the molar extinction coefficient of PpIX at the two wavelengths and the fact that only a portion of the emission spectrum is measureable with red light excitation. This reality was exacerbated by the poor tolerances often found in budget 635-nm laser diodes, which often operate at laser peaks in the 637- to 640-nm range. A laser diode emitting closer to 633 nm could reduce the red channel detectable limit by more than a factor of 4.

Phantom measurements also showed that the PpIX fluorescence estimates were insensitive to changes in optical properties,

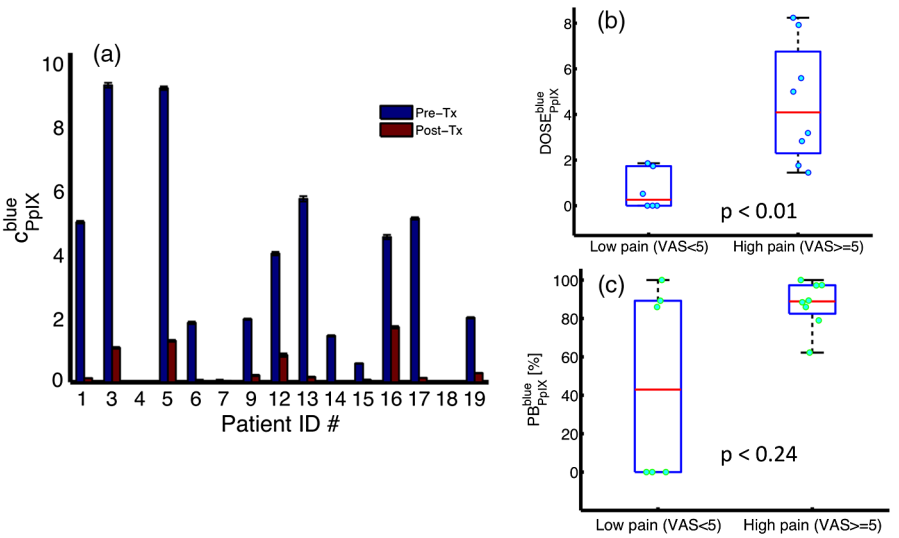

Fig. 8 PpIX fluorescence measured in response to blue excitation. (a) Patient-specific fitted PpIX fluorescence pre- and post-Tx. Box-plots show comparison of (b) absolute PDT dose and (c) percent PpIX photobleaching with patient reporting low pain (VAS < 5) and high pain (VAS >= 5).

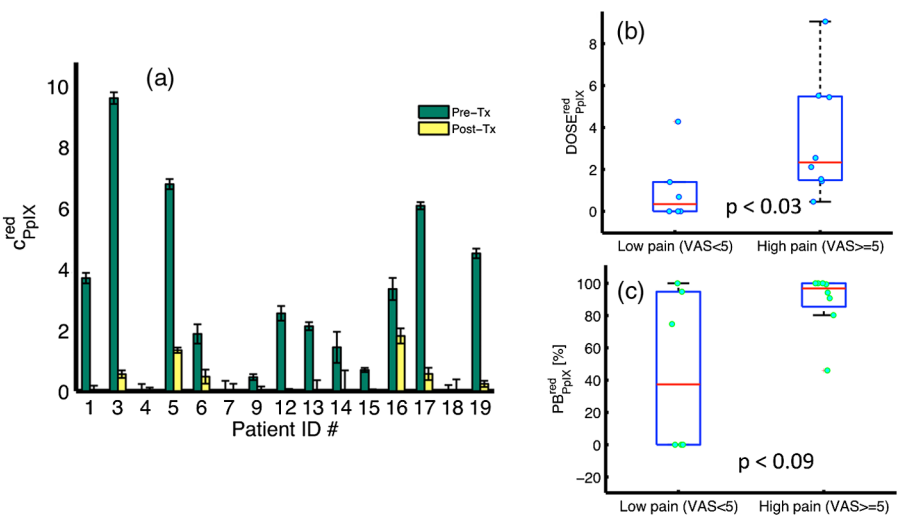

Fig. 9 PpIX fluorescence measured in response to red excitation. (a) Patient-specific fitted PpIX fluorescence pre- and post-Tx. Box-plots show comparison of (b) absolute PDT dose and (c) percent PpIX photobleaching with patient reporting low pain (VAS < 5) and high pain (VAS >= 5).

provided a white-light-based correction was applied. Raw fluorescence remission measured with either blue or red light excitation was sensitive to background properties, with observed errors topping 60 and 30%, respectively, over a biologically relevant range of optical properties. Applying an empirical correction approach reduced these errors substantially, with remaining errors of <10%. It is important to note that the empirical optical property correction applied to these measurements was valid only for the fiber geometry and range of optical properties investigated, and was not directly generalizable to other geometries or sets of properties. A key consideration when interpreting the clinical data set was whether the remitted spectra were sensitive to the form of the scattering phase function for our small source detector separation (SD). Inspection of the μ_s' estimates in Fig. 10 showed that $\mu_s'SD > 0.5$ at 639 nm for the majority of patients, which has been defined[37] as a threshold value for sensitivity to phase function effects. Therefore, the high scattering regime of skin allowed accurate analysis of reflectance without independent estimation of μ_s' and moments of the phase function. These factors support the use of the correction factor validated in phantoms to correct clinical measurements. Importantly, this correction allows direct comparison of PpIX fluorescence measurements between patients.

The pilot clinical study was performed to establish the feasibility of integrating the device into the clinical workflow of a dermatology practice and to report initial correlates between measurements and patient-reported pain. Standard of care ALA-incubation times varied widely among clinics and a short ALA incubation schedule was used in this study, which is 1 h between ALA and light administration. An important clinical observation was the interpatient variability in PpIX production, with some patients showing undetectable levels of PpIX while others

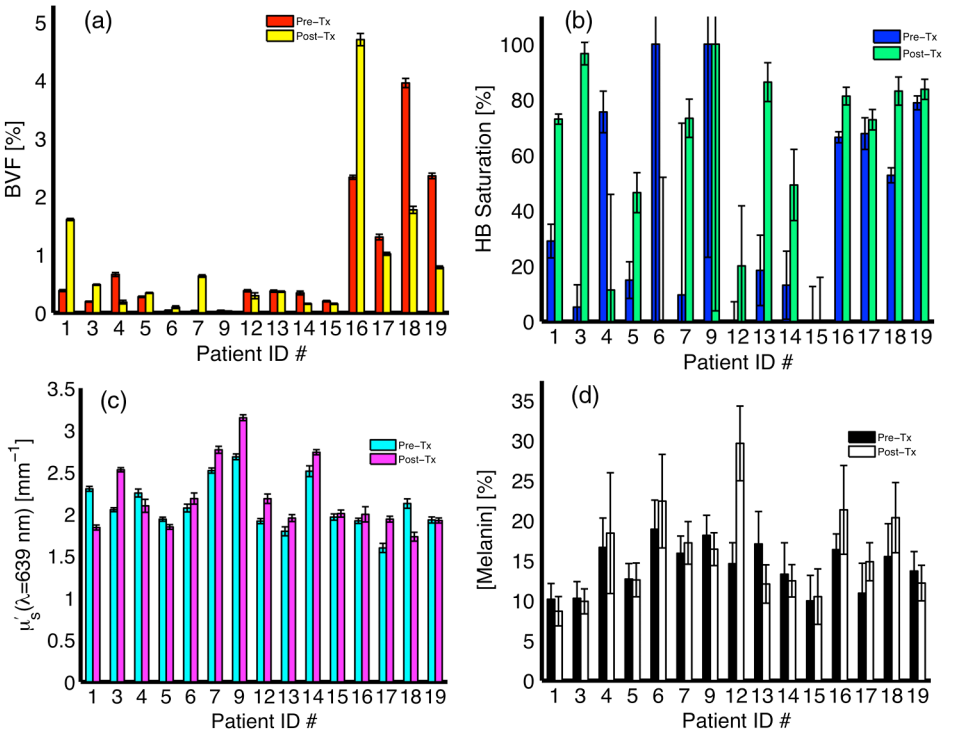

Fig. 10 Patient-specific optical parameters measured before and after PpIX PDT treatment: (a) blood volume fraction, (b) microvascular saturation, (c) reduced scattering coefficient at 637 nm, and (d) volume fraction of melanocytes in the epidermis.

produced an extremely robust response. Long-term clinical outcome response data were not part of this initial data set, and thus, we used patient-reported pain as a surrogate correlation parameter, which has been shown to be roughly proportional to PpIX fluorescence prior to illumination[47] and proportional to erythema following treatment.[48] Using this metric, the PpIX fluorescence after 1-h ALA incubation was significantly higher (in the aggregate) in patients reporting high pain than those reporting low pain. This relationship was also observed for total absolute change in fluorescence before and after light dose delivery, though not for relative percent change. These results were consistent for both blue and red light excitation. It should be noted that VAS pain was only an implicit metric for therapeutic dose and is also dependent on the nerve density within the treated tissue, which was not evaluated in this study. But overall, these data suggest that the dosimeter measurements may have the potential to stratify patients who produced high and low levels of PpIX after a short incubation time.

The core aspect of our new two-channel excitation fluorescence dosimeter that is unique within the field of ALA-PpIX PDT monitoring is the ability to quantify PpIX originating from different depths. A series of Monte Carlo simulations were performed to characterize the sensitivity of red and blue fluorescence measurements to depth distribution of PpIX in the skin. Simulation results showed the red channel samples PpIX from deeper locations than the blue. This result is expected, given the increased absorption and scattering experienced by blue light compared with red light in skin. The simulations also showed that the ratio of the red to blue fluorescence was sensitive to the depth-dependent distribution of PpIX. The ratio data from simulations normalized the red and blue collected intensities for the case of homogenously distributed PpIX, and changes in the normalized ratio resulted from changing the spatial distribution of PpIX within the modeled tissue volume. An increased ratio of red to blue indicated an increased contribution of PpIX from relatively deeper locations, while a decreased ratio indicated more PpIX in the superficial layers of the skin. The ratio of red to blue fluorescence signals observed *in vivo* was [0.23 to 2.2]. While slight variations in this ratio may be caused by imperfect correction for optical property effects, the data in Fig. 5 suggest that optical property based error is likely to be ~20% and is unlikely to explain the 10-fold range of ratio values observed in patients. Thus, the differences in the observed ratio suggest differences in the depth-dependent distribution of PpIX among patients. Interestingly, the clinical data showed that lower $Ratio_{RB}$ values, indicating more superficial PpIX, were associated with higher amounts of reported pain. It is important to note that patients in this study were treated with blue light, hypothetically increasing the product of PpIX concentration and light fluence in the superficial layers of tissue. It should be noted that the number of patients included in the ratio analysis in Fig. 10 is limited, and robust conclusions on this topic require an expanded patient population. Future studies will consider the potential use of $Ratio_{RB}$ as a dosimetric parameter.

The white light measurements provided quantitative description of local vascular physiology and the changes that occur during treatment. Comparison of the range of tissue parameters estimated in Fig. 11 are consistent with previous descriptions of skin tissue.[30] While there were some trends observed between changes in BVF, Sat, pain, and the PDT dose, patients showed a large amount of variability both in pretreatment parameters and the changes experienced during treatment. It is well understood that changes in perfusion may occur dynamically during treatment,[35] and sampling at discrete times before and after treatment may, in fact, miss tissue response that occurs during

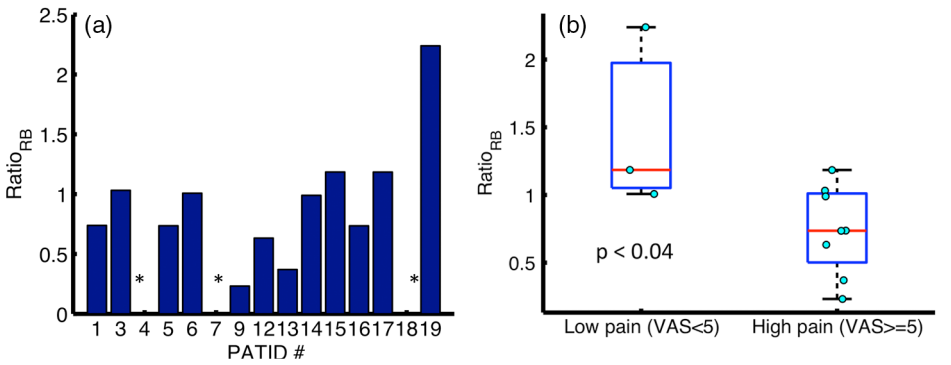

Fig. 11 Patient-specific ratio of red to blue PpIX fluorescence; * marks indicate zero PpIX. Box-plot shows comparison of ratio with patient reporting low pain (VAS < 5) and high pain (VAS >= 5).

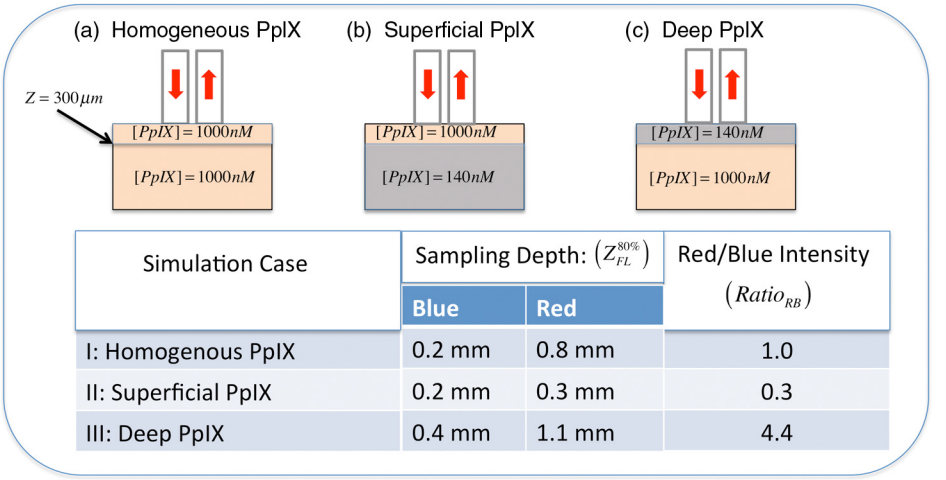

Simulation Case	Sampling Depth: $(Z_{FL}^{80\%})$		Red/Blue Intensity $(Ratio_{RB})$
	Blue	Red	
I: Homogenous PpIX	0.2 mm	0.8 mm	1.0
II: Superficial PpIX	0.2 mm	0.3 mm	0.3
III: Deep PpIX	0.4 mm	1.1 mm	4.4

Fig. 12 Monte Carlo simulation data showing influence of PpIX depth distribution on the sampled depth of fluorescence origin and the ratio of collected light intensities. Three distributions were considered: (a) uniform PpIX throughout, (b) superficial PpIX, and (c) deep PpIX. The 80% fluorescence sampling depth is reported for blue and red excitation channels, and the red/blue ratio is given for each case.

illumination. More informative descriptions of tissue response may be found by sampling either at times during the illumination, or sampling over a window following treatment to better characterize the regional changes to perfusion and/or edema.

The results reported here are encouraging, but require further validation in a prospective clinical study. Assuming the dosimeter measurements prove to be predictive of response, additional interventions may be applied to improve outcome, such as extending ALA-incubation time or administering an adjuvant to increase PpIX production. However, the initial development and validation of the multifunction dosimeter, described in this report, is a first step toward making clinical PDT treatments of skin precancers (i.e., AKs) more predictable and hopefully more controllable.

Acknowledgments

The authors would like to thank Jason R. Gunn for help in optical phantom preparation, Karen L. Sheehan for many clinical measurements with the dosimeter, and Professor Steven L. Jacques (Oregon Health and Science University) for helpful conversations about tissue optics and modeling of light signals. This work was funded by grants P01 CA084203 and K25 CA164248-01.

References

1. E. W. Jeffes, "Levulan: the first approved topical photosensitizer for the treatment of actinic keratosis," *J. Dermatol. Treat.* **13**(Suppl 1), S19–23 (2002).
2. S. R. Feldman and A. B. Fleischer Jr., "Progression of actinic keratosis to squamous cell carcinoma revisited: clinical and treatment implications," *Cutis* **87**(4), 201–207 (2011).
3. E. W. Jeffes et al., "Photodynamic therapy of actinic keratoses with topical aminolevulinic acid hydrochloride and fluorescent blue light," *J. Am. Acad. Dermatol.* **45**(1), 96–104 (2001).
4. D. J. Piacquadio et al., "Photodynamic therapy with aminolevulinic acid topical solution and visible blue light in the treatment of multiple actinic keratoses of the face and scalp: investigator-blinded, phase 3, multicenter trials," *Arch. Dermatol.* **140**(1), 41–46 (2004).
5. E. H. Tschen et al, "Photodynamic therapy using aminolaevulinic acid for patients with nonhyperkeratotic actinic keratoses of the face and scalp: phase IV multicentre clinical trial with 12-month follow up," *Br. J. Dermatol.* **155**(6), 1262–1269 (2006).
6. J. C. Kennedy and R. H. Pottier, "Endogenous protoporphyrin IX, a clinically useful photosensitizer for photodynamic therapy," *J. Photochem. Photobiol. B Biol.* **14**(4), 275–292 (1992).
7. T. Smits et al., "Correlation between macroscopic fluorescence and protoporphyrin IX content in psoriasis and actinic keratosis following application of aminolevulinic acid," *J. Investig. Dermatol.* **125**(4), 833–839 (2005).
8. M. Tarstedt et al., "A randomized multicenter study to compare two treatment regimens of topical methyl aminolevulinate (Metvix)-PDT

in actinic keratosis of the face and scalp," *Actadermato-venereologica* **85**(5), 424–428 (2005).
9. Q. Peng et al., "Selective distribution of porphyrins in skin thick basal cell carcinoma after topical application of methyl 5-aminolevulinate," *J. Photochem. Photobiol. B Biol.* **62**(3), 140–145 (2001).
10. S. Smith et al., "Short incubation PDT versus 5-FU in treating actinic keratoses," *J. Drugs Dermatol.* **2**(6), 629–635 (2003).
11. L. R. Braathen et al., "Short incubation with methyl aminolevulinate for photodynamic therapy of actinic keratoses," *J. Eur. Acad. Dermatol. Venereol.* **23**(5), 550–555 (2009).
12. R. Bissonnette et al., "Short incubation photodynamic therapy with methylaminolevulinate and no occlusion for the treatment of actinic keratoses," *J. Am. Acad. Dermatol.* **67**(6), 1386–1387 (2012).
13. D. Touma et al., "A trial of short incubation, broad-area photodynamic therapy for facial actinic keratoses and diffuse photodamage," *Arch. Dermatol.* **140**(1), 33–40 (2004).
14. C. Fritsch et al., "Optimum porphyrin accumulation in epithelial skin tumours and psoriatic lesions after topical application of delta-aminolaevulinic acid," *Br. J. Cancer* **79**(9–10), 1603–1608 (1999).
15. A. L. Golub et al., "The monitoring of ALA-induced protoporphyrin IX accumulation and clearance in patients with skin lesions by in vivo surface-detected fluorescence spectroscopy," *Laser Med. Sci* **14**(2), 112–122 (1999).
16. A. K. Sinha et al., "Methotrexate used in combination with aminolaevulinic acid for photodynamic killing of prostate cancer cells," *Br. J. Cancer* **95**(4), 485–495 (2006).
17. M. J. Gerritsen et al., "Pretreatment to enhance protoporphyrin IX accumulation in photodynamic therapy," *Dermatology* **218**(3), 193–202 (2009).
18. B. C. Wilson, M. S. Patterson, and L. Lilge, "Implicit and explicit dosimetry in photodynamic therapy: a new paradigm," *Lasers Med. Sci.* **12**(3), 182–199 (1997).
19. C. Sheng et al., "Photobleaching-based dosimetry predicts deposited dose in ALA-PpIX PDT of rodent esophagus," *Photochem. Photobiol.* **83**(3), 738–748 (2007).
20. K. R. Rollakanti et al., "Techniques for fluorescence detection of protoprophyrin IX in skin cancers associated with photodynamic therapy," *Photon Lasers Med* **2**(4), 287–303 (2013).
21. K. Rick et al., "Pharmacokinetics of 5-aminolevulinic acid-induced protoporphyrin IX in skin and blood," *J. Photochem. Photobiol. B* **40**(3), 313–319 (1997).
22. J. Hewett et al., "The application of a compact multispectral imaging system with integrated excitation source to in vivo monitoring of fluorescence during topical photodynamic therapy of superficial skin cancers," *Photochem. Photobiol.* **73**(3), 278–282 (2001).
23. S. H. Ibbotson et al., "Characteristics of 5-aminolaevulinic acid-induced protoporphyrin IX fluorescence in human skin in vivo," *Photodermatol. Photoimmunol. Photomed.* **22**(2), 105–110 (2006).
24. C. B. Warren et al., "Noninvasive fluorescence monitoring of protoporphyrin IX production and clinical outcomes in actinic keratoses following short-contact application of 5-aminolevulinate," *J. Biomed. Opt.* **15**(5), 051607 (2010).
25. F. Piffaretti et al., "Correlation between protoporphyrin IX fluorescence intensity, photobleaching, pain and clinical outcome of actinic keratosis treated by photodynamic therapy," *Dermatology* **227**(3), 214–225 (2013).
26. B. W. Pogue and G. Burke, "Fiber-optic bundle design for quantitative fluorescence measurement from tissue," *Appl. Opt.* **37**(31), 7429–7436 (1998).
27. A. Amelink et al., "Quantitative fluorescence spectroscopy in turbid media using fluorescence differential path length spectroscopy," *J. Biomed. Opt.* **13**(5), 054051 (2008).
28. S. C. Kanick et al., "Extraction of intrinsic fluorescence from single fiber fluorescence measurements on a turbid medium," *Opt. Lett.* **37**(5), 948–950 (2012).
29. A. Kim et al., "Quantification of in vivo fluorescence decoupled from the effects of tissue optical properties using fiber-optic spectroscopy measurements," *J. Biomed. Opt.* **15**(6), 067006 (2010).
30. S. L. Jacques, "Optical properties of biological tissues: a review," *Phys. Med. Biol.* **58**(11), R37–61 (2013).
31. P. A. Valdes et al., "A spectrally constrained dual-band normalization technique for protoporphyrin IX quantification in fluorescence-guided surgery," *Opt. Lett.* **37**(11), 1817–1819 (2012).
32. R. B. Saager et al., "Quantitative fluorescence imaging of protoporphyrin IX through determination of tissue optical properties in the spatial frequency domain," *J. Biomed. Opt.* **16**(12), 126013 (2011).
33. U. Sunar et al., "Quantification of PpIX concentration in basal cell carcinoma and squamous cell carcinoma models using spatial frequency domain imaging," *Biomed. Opt. Express* **4**(4), 531–537 (2013).
34. B. P. Flynn et al., "White light-informed optical properties improve ultrasound-guided fluorescence tomography of photoactive protoporphyrin IX," *J. Biomed. Opt.* **18**(4), 046008 (2013).
35. T. L. Becker et al., "Monitoring blood flow responses during topical ALA-PDT," *Biomed. Opt. Express* **2**(1), 123–130 (2010).
36. T. A. Middelburg et al., "Monitoring blood volume and saturation using superficial fibre optic reflectance spectroscopy during PDT of actinic keratosis," *J. Biophotonics* **4**(10), 721–730 (2011).
37. S. C. Kanick et al., "Scattering phase function spectrum makes reflectance spectrum measured from Intralipid phantoms and tissue sensitive to the device detection geometry," *Biomed. Opt. Express* **3**(5), 1086–1100 (2012).
38. R. Michels, F. Foschum, and A. Kienle, "Optical properties of fat emulsions," *Opt. Express* **16**(8), 5907–5925 (2008).
39. N. Rajaram et al., "Experimental validation of the effects of microvasculature pigment packaging on in vivo diffuse reflectance spectroscopy," *Lasers Surg. Med.* **42**(7), 680–688 (2010).
40. I. V. Meglinski and S. J. Matcher, "Quantitative assessment of skin layers absorption and skin reflectance spectra simulation in the visible and near-infrared spectral regions," *Physiol. Meas.* **23**(4), 741–753 (2002).
41. A. Amelink, D. J. Robinson, and H. J. Sterenborg, "Confidence intervals on fit parameters derived from optical reflectance spectroscopy measurements," *J. Biomed. Opt.* **13**(5), 054044 (2008).
42. J. C. Finlay et al., "Porphyrin bleaching and PDT-induced spectral changes are irradiance dependent in ALA-sensitized normal rat skin in vivo," *Photochem. Photobiol.* **73**(1), 54–63 (2001).
43. E. Hull et al., "Noninvasive, optical detection of diabetes: model studies with porcine skin," *Opt. Express* **12**(19), 4496–4510 (2004).
44. R. Weersink et al., "Noninvasive measurement of fluorophore concentration in turbid media with a simple fluorescence/reflectance ratio technique," *Appl. Opt.* **40**(34), 6389–6395 (2001).
45. B. Kruijt et al., "Monitoring ALA-induced PpIX photodynamic therapy in the rat esophagus using fluorescence and reflectance spectroscopy," *Photochem. Photobiol.* **84**(6), 1515–1527 (2008).
46. A. K. Glaser et al., "A GAMOS plug-in for GEANT4 based Monte Carlo simulation of radiation-induced light transport in biological media," *Biomed. Opt. Express* **4**(5), 741–759 (2013).
47. S. K. Attili, R. Dawe, and S. Ibbotson, "A review of pain experienced during topical photodynamic therapy—our experience in Dundee," *Photodiagnosis Photodyn. Ther.* **8**(1), 53–57 (2011).
48. S. Fabricius et al., "The relation between methyl aminolevulinate concentration and inflammation after photodynamic therapy in healthy volunteers," *Photochem. Photobiol. Sci.* **12**(1), 117–123 (2013).

Stephen Chad Kanick is an assistant professor of engineering at Dartmouth College. He holds a doctoral degree in chemical engineering from the University of Pittsburgh and completed a postdoctoral appointment at the Erasmus Medical Center in Rotterdam, The Netherlands. His research focuses on the development of quantitative spectroscopic approaches to diagnose pathologies, guide surgeries, and monitor administered therapies. He is the recipient of a career development award from the National Cancer Institute.

Scott C. Davis is an assistant professor of engineering at Dartmouth College and holds degrees in physics, mechanical, and biomedical engineering. His research aims to develop and assess new optical imaging technologies to diagnose tissue and guide cancer therapy. He has published over 40 peer-reviewed articles and currently directs a National Cancer Institute funded research project to develop multi-tracer deep-tissue optical imaging techniques to quantify molecular biomarkers *in vivo*.

Yan Zhao received his BS degree in electronic science and technology from Xi'an Jiaotong University, Xi'an, China, in 2012. He is currently working toward his PhD degree from Thayer School of Engineering, Dartmouth College in Hanover, New Hampshire. His research interests include biomedical spectroscopy and imaging.

Tayyaba Hasan is a professor of dermatology at Wellman Center for Photomedicine, Harvard Medical School and a professor of health sciences and technology (Harvard-MIT). Her research is directed to basic and translational studies in photochemistry, photobiology, and PDT. She has over 250 publications and several patents, and is the recipient of several science and mentoring awards.

Edward V. Maytin is a board-certified dermatologist in the Departments of Dermatology, and of Biomedical Engineering, at the Cleveland Clinic in Cleveland, Ohio. He holds an MD degree and a PhD degree in radiation biology and biophysics from the University of Rochester, New York, and currently runs a specialty clinic for PDT of skin cancer and also directs a laboratory research program (funded by the National Cancer Institute) on biochemical mechanisms of PDT.

Brian W. Pogue is a professor of engineering, physics, and astronomy at Dartmouth College, and an adjunct professor of surgery at the Geisel School of Medicine. He has a doctoral degree in medical physics from McMaster University in Canada. His research is in optical imaging systems, with a focus on molecular and structural imaging of cancer for surgical guidance and imaging radiation therapy and is funded by several grants from the National Cancer Institute.

M. Shane Chapman is the section chief of dermatology and an associate professor of dermatology in the Department of Surgery at Dartmouth-Hitchcock Medical Center (DHMC) and the Geisel School of Medicine at Dartmouth, in Lebanon and Hanover, New Hampshire. He is the director of clinical trials in dermatology at DHMC.